


Effects of calcium on planar fault energies in ternary magnesium alloys

E. I. Andritsos* and A. T. Paxton

Department of Physics, King's College London, Strand, London, WC2R 2LS, United Kingdom

 (Received 31 August 2018; revised manuscript received 22 November 2018; published 16 January 2019)

We are motivated by the need to design magnesium alloys that are free of rare-earth additions, but, nevertheless, forgeable and free of strong basal texture. It has become recently clear that calcium is a promising candidate to replace the economically strategic rare-earth elements. To this end, we focus on the planar faults that typically bound partial glide dislocations of the hcp lattice. We have made first-principles calculations to examine the generalized stacking fault energy (SFE) of the basal, first- and second-order pyramidal planes. We examine the changes in fault energy and anisotropy for increasing alloy concentrations and the effect of low concentrations of calcium. For the calculation of the SFEs from first principles, we use the non-self-consistent Harris-Foulkes approximation to the local density functional theory. We demonstrate that while this approximation leads to high computational efficiency, there is no significant loss of precision compared to the self-consistent Hohenberg-Kohn functional. We go beyond all previous work in which the alloying element is assumed to reside *within* the fault and instead address the more realistic situation in which the SFE is modified by the *remote* presence of the impurity. This allows us to determine whether segregation is expected and we find that while elements do segregate to the basal fault they do not to pyramidal faults. Nevertheless, in either case, the fault energy is strongly modified by alloying. This argues that either a long-ranged electronic structure effect is in play, or the fault energy modification is affected by the atomic size difference—particularly large in the case of Ca. We find that Mg-Li-Ca and Mg-Zn-Ca alloys show a remarkable decrease in anisotropy, which is consistent with their known high strength and formability. In favorable cases, this comes about by *strengthening* basal slip rather than *weakening* nonbasal slip. The Ca contribution increases inversely with the atomic size of the alloying element, allowing us to speculate that alloying effects are generally atomic size effects.

DOI: [10.1103/PhysRevMaterials.3.013607](https://doi.org/10.1103/PhysRevMaterials.3.013607)

I. INTRODUCTION

Magnesium-based alloys are widely used in the automotive and aerospace industries due to their high strength and light weight. It is known that Mg alloys suffer from low tensile ductility, high plastic anisotropy, strong texture, and low corrosion resistance. To tackle those problems, a small percentage of rare earth is usually added in most commercial alloys. Depending on the manufacturing process and the composition of the alloy, addition of rare earths shows enhancement in one or more properties such as improved ductility, hardness, high-temperature strength and formability, lower basal texture, and creep and corrosion resistance [1–10]. Reports indicate that the main reason of improvement is due to the strong segregation of rare earths to dislocations and grain boundaries [11–14]. Still, the underlying mechanism of rare-earth enhancement of mechanical properties is not well understood at the atomic level.

For economic reasons, of even greater importance is to find alloying additions that are not strategic metals which have the same beneficial properties as rare earths. A few non-rare-earth elements such as lithium, zinc, and calcium have been identified to strengthen the basal plane and increase nonbasal activity [14–17], and generally improve the mechanical properties of Mg alloys. In particular, Mg alloys

with a low concentration of Ca have been found to enhance mechanical properties similarly to rare earths, identifying Ca as a potentially good rare-earth substitute. Depending on the production method and the alloy concentration, Ca in Mg alloys may improve strength, tensile ductility, stretch formability and creep resistance, and lower the basal texture [18–26].

It is rather clear that the heart of the problem of strong basal texture development and plastic anisotropy is the tendency for easy glide to occur only on the basal planes. This means that in the absence of twinning (and observed twinning modes in Mg offer an order of magnitude smaller shear than other hcp metals) Von Mises's criterion for general yield is not met. After detailed atomic scale calculations, Curtin and co-workers [27–29] have shown that glide on nonbasal planes involves complex processes of constriction, cross-slip and core transformations occurring on long timescales; and that these processes, in particular cross slip, are very sensitive to the presence of alloying elements. A key quantity is the stacking fault energy on basal, prism, and pyramid planes. An obvious goal in alloy design is to find combinations of nonstrategic alloy elements that, partly through their effects on stacking fault energies, can bring about a hardening of the basal planes to slip while at the same time facilitating glide on nonbasal planes.

In this study we focus on Mg alloys with Ca, Li, and Zn additions, in order to bring out the large potential of these alloys. While calculations of fault energies in binary

*lefteri.andritsos@kcl.ac.uk

[28,30–33] and a few ternary [31,34,35] Mg alloys already exist, here we make four major contributions. (1) We extend the range of compositions and SFE calculations of Mg-based ternary alloys. (2) We consider the more realistic situation that previously has not been done, in which the alloy elements are not positioned *at* the fault plane. This means that we can understand the long-ranged effects of the alloying elements on fault energies and at the same time calculate an effective segregation energy. (3) We demonstrate the use of a particularly efficient approximation in the density functional theory, which accelerates calculations of large unit cells with no significant loss of precision. (4) We attempt to separate out electronic structure effects from size effects in the roles of alloying elements in modifying fault energies.

We present results for the stable stacking fault energies (γ_{sf}) of three ternary alloys, Mg-Li-Ca, Mg-Zn-Ca, and Mg-Y-Ca, in four different concentrations each. We make high-efficiency density functional theory (DFT) calculations to study the SFEs along the three major glide planes for Mg, the basal, and first- (I) and second- (II) order pyramidal planes. In Sec. III, we analyze our results in four subsections: (1) the effect of increasing alloying element concentration (Li, Zn, or Y) in the alloy. (2) The change in the anisotropy of mechanical properties based on the ratio of the pyramidal over basal stable SFEs. (3) The effect of proximity of Ca to the fault on the SFEs. (4) The basal-plane contribution of Ca in the three ternary alloys by comparing with calculations for binary alloys without Ca.

II. HIGH EFFICIENCY NON SELF-CONSISTENT CALCULATIONS

Efficiency for DFT calculations is very important, especially for large or nonequilibrium systems which are highly computationally demanding. In our total-energy calculations, we employ the so-called non-self-consistent (sc) Harris-Foulkes (HF) approximation. In the sc limit, the functional of Harris [36] and Foulkes [37] is identical to the Hohenberg-Kohn functional [38,39]. However, the former is a functional only of a trial input electron density and, moreover, the HF functional evaluated for a trial input density is correct to second order in the difference between the trial and sc charge densities. With a choice of neutral overlapping atomic densities, the non-sc approximation has been frequently investigated [40–46] and found to produce accurate total energies for bulk and surface systems. By calculating total energy and interatomic forces in the HF approximation, we avoid the need for lengthy sc iterations.

The stacking faults are translation defects, which can be constructed notionally by making an infinite cut parallel to a crystallographic plane and displacing the crystal on one side of the cut with respect to the other by a translation $s\mathbf{T}$. \mathbf{T} lies in the direction of the stacking fault and s is a number between 0 and 1. Hence the most efficient way of studying planar faults is by using the supercell model to create a single-fault cell with homogeneous shear boundary conditions (HSBC). In HSBC, the crystal is displaced by $s\mathbf{T}$ but the atoms are fixed to their initial positions. The stacking-fault is created at the interface of the supercell with its periodic image, at the fault plane. With the single-fault cell, we need a smaller supercell along the

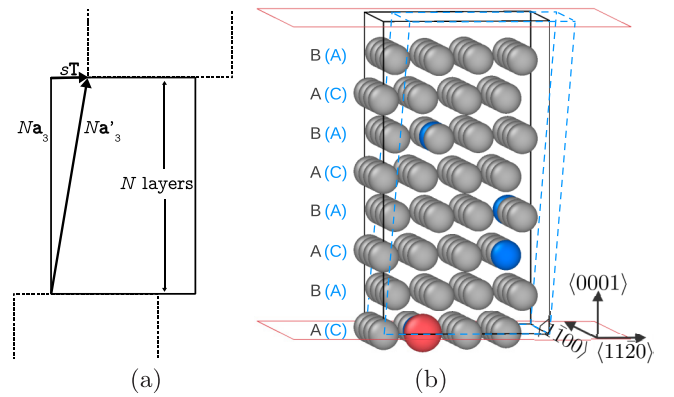


FIG. 1. The left figure shows the homogeneous shear boundary conditions we use for the construction of planar faults. Na_3 is the initial supercell vector, noncoplanar to the stacking fault surface. Na'_3 is the final supercell vector translated by $s\mathbf{T}$, where s takes a value between 0 and 1. The dashed lines represent the periodic images of the supercell in the direction perpendicular to the stacking fault plane. This method allows us to use fewer N layers and boost efficiency in our calculations. The right figure represents the basal configuration of the tLi_4 alloy. The black solid lines describe a supercell without a stacking fault and the blue dashed lines a supercell with a stacking fault. The red rectangles show the planar fault. A, B, and C express the stacking sequence of the planes in the direction perpendicular to the stacking fault plane. The stacking sequence for a supercell with a stacking fault is ...ABABCACA.... The silver spheres represent the Mg atoms, the blue the Li atoms, and the red is the Ca atom. In this case, the Ca atom is placed at the stacking fault (interface). The SQS method is used for allocating the Li atoms in the supercell.

direction normal to the stacking-fault (γ) surface (N layers) than in the double-fault cell [or “slab” model ($2N$ layers)], which is often described in literature. We apply discrete shear parallel to the γ surface, in the direction of the stacking fault, and allow atomic relaxation only along the direction perpendicular to it. This type of relaxation, along the direction perpendicular to the γ surface was initially described by Vitek [47]. We show a typical HSBC construction in Fig. 1(a). We apply periodic boundary conditions in all directions.

In all our calculations, the stacking fault plane is defined by \mathbf{a}_1 and \mathbf{a}_2 . \mathbf{a}_3 is either exactly, or very nearly, perpendicular to the γ surface. \mathbf{a}_1 , \mathbf{a}_2 , and \mathbf{a}_3 are the lattice vectors of the unit cell and vary depending on the studied stacking fault plane. The unit cell with stacking fault has unit vectors \mathbf{a}_1 , \mathbf{a}_2 , and \mathbf{a}'_3 , where $\mathbf{a}'_3 = \mathbf{a}_3 + s\mathbf{T}$, while the atom positions are kept the same as in the cell without a stacking fault. We calculate the SFE of each plane, as the total energy difference of a supercell with a stacking fault and a supercell without a stacking fault divided by the stacking fault area.

In Fig. 1(b), we visualize a typical supercell for calculations of the SFE. This supercell depicts the basal configuration of tLi_4 alloy, as described in Table I. The silver spheres represent Mg atoms, the blue Li atoms and the red a Ca atom. The black solid lines represent the supercell box without a stacking fault and the blue dashed lines the supercell box with a stacking fault. The red rectangles represent the γ surface. The letters A and B show the stacking sequence of the supercell without a stacking fault. For the case with stacking

TABLE I. Various compositions of the studied Mg-Li/Zn/Y-Ca alloys. In order are the reference name for each alloy (the subscript shows the number of Li/Zn/Y atoms in a 128-atom configuration), the atomic and weight percentage.

| Name | at% | wt% |
|-------------------|-------------------|-------------------|
| tLi ₁ | Mg-0.78Li-0.78Ca | Mg-0.22Li-1.29Ca |
| tLi ₂ | Mg-1.56Li-0.78Ca | Mg-0.45Li-1.30Ca |
| tLi ₄ | Mg-3.13Li-0.78Ca | Mg-0.91Li-1.31Ca |
| tLi ₁₇ | Mg-13.28Li-0.78Ca | Mg-4.17Li-1.42Ca |
| tZn ₁ | Mg-0.78Zn-0.78Ca | Mg-2.06Zn-1.27Ca |
| tZn ₂ | Mg-1.56Zn-0.78Ca | Mg-4.07Zn-1.25Ca |
| tZn ₃ | Mg-2.34Zn-0.78Ca | Mg-6.04Zn-1.23Ca |
| tZn ₂₂ | Mg-17.19Zn-0.78Ca | Mg-35.69Zn-0.99Ca |
| tY ₁ | Mg-0.78Y-0.78Ca | Mg-2.79Y-1.26Ca |
| tY ₂ | Mg-1.56Y-0.78Ca | Mg-5.46Y-1.23Ca |
| tY ₃ | Mg-2.34Y-0.78Ca | Mg-8.03Y-1.21Ca |
| tY ₆ | Mg-4.69Y-0.78Ca | Mg-15.18Y-1.14Ca |

fault, the supercell has ...ABAB... stacking sequence and its periodic image ...CACA..., in the direction perpendicular to the γ surface. Therefore the stacking fault plane lies between B and C layer and the stacking sequence is ...ABABCACA.... The first-order pyramidal plane is corrugated and defines closely (narrow) and loosely (wide) spaced planes. For the first-order pyramidal plane, we only consider stable SFE of the widely spaced planes. Translation along the wide planes is known to produce much lower SFE than in narrow planes, hence it is more relevant to this study.

To examine the accuracy and efficiency of our non-sc calculations we compare the basal-plane SFEs for a 24-atom Mg supercell calculated with the non sc HF and sc HKS functionals. We calculate the total energy with the full-potential linear muffin-tin orbital (FP-LMTO) method as implemented in the Questaal suite [48]. We use the PBE generalized gradient approximation (GGA) to calculate the exchange and correlation potential. The 24-atom supercell size is $\sqrt{3}a \times a \times 6c$ and the Brillouin zone (BZ) is sampled by a large \mathbf{k} -point mesh of $23 \times 40 \times 4$, using the well known Monkhorst-Pack scheme. For all our calculations we use a lattice constant $a = 6.041$ au (3.197 Å) and keep the c/a ratio fixed to $c/a = 1.627$.

We have thoroughly examined the effect of various computational parameters, such as the supercell size, the number of \mathbf{k} points, the integration of the BZ, and energy and charge density convergence criteria on the SFE. The effect of the supercell size in the calculation of the SFE has been identified and explored by Wang *et al.* [49], showing a large dependency. Their results show a decrease in the SFE of $\sim 27\%$ of the initial value as the supercell size doubles. We have tested the effect of the number of atoms in the supercell (24, 28, and 32 atoms) for the same planar fault and number of \mathbf{k} points. The difference in basal stable stacking fault energy (γ_{sf}) of a 24-atom supercell (four basis atoms in $1 \times 1 \times 6$ unit cell stacking) and a 32-atom supercell (four basis atoms in $1 \times 1 \times 8$ unit cell stacking) is almost negligible (~ 1.2 mJ/m²). Moreover, for the 24-atom supercell, we performed total energy calculations for a set of different number of \mathbf{k} points, from 6 to 48 for the x and y direction and from 1 to 20 for the z direction. We found

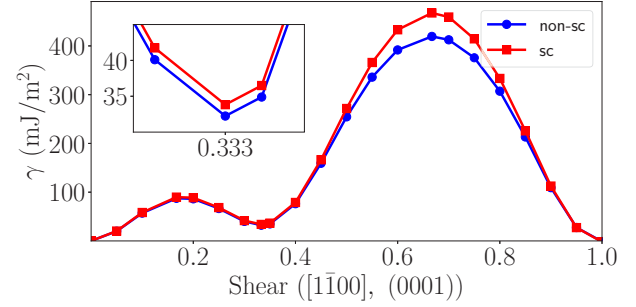


FIG. 2. SFEs of the basal plane for pure Mg calculated with the non-sc approximation, compared with results from sc calculations. The two different functionals predict comparable energies for the same supercell. At low SFEs, the difference amounts only a few mJ/m², while it increases at higher SFEs, exhibiting an error of 10.3% at the second γ_{sf} .

that a minimum of a $12 \times 20 \times 2$ \mathbf{k} -point mesh is needed for convergence of less than 1 mJ/m² change in γ_{sf} .

In Fig. 2, we present the SFEs along the $[1\bar{1}00]$ direction in the basal plane as calculated with the sc and the non-sc approximations. The two approximations give comparable results, especially at low SFEs. The differences in the calculated SFEs at the first unstable stacking fault (γ_{usf}) at $1/6[1\bar{1}00]$ is 2.4 mJ/m² (2.6%), the γ_{sf} at $1/3[1\bar{1}00]$ is 1.6 mJ/m² (2.6%) and the second γ_{usf} at $2/3[1\bar{1}00]$ is 48.2 mJ/m² (10.3%). The increasing error for high SFEs is due to the overlap of the atomic spheres (usually for overlap higher than 10% of the internuclear distance), as constructed in the FP-LMTO method. All calculations in the next section regard stable stacking faults and we expect only a small deviation in our results. The accuracy of the non-sc method is similar to that of the sc method, which is considered as the standard method in DFT calculations. In addition to the good agreement with the sc method, the non-sc method achieves at least six times lower computational cost for total energy calculations, efficiency similar to that of previous reports [46].

III. RESULTS AND DISCUSSION

For the calculation of all SFEs for binary and ternary Mg alloys, we use a 128-atom supercell. The supercell dimensions are $2\sqrt{3}a \times 4a \times 4c$ for the basal plane, $2(c+a) \times 2a \times \sim 12.2a$ for the first-order pyramidal plane, and $2(c+a) \times 2\sqrt{3}a \times \sim 6.8a$ for the second-order pyramidal plane. The pyramidal structures have been constructed following Frank's four-dimensional vectors method [50]. According to this method, the \mathbf{a}_3 corresponds to $\mathbf{a}_3 = \cos(\theta)|\mathbf{a}_3^p|/|\mathbf{a}_1|$, where $|\mathbf{a}_3^p| = \cos(\theta^p)c/a$; θ^p is the characteristic angle of the pyramidal plane $[\tan(c/a)]$ and θ is the angle of the projection of \mathbf{a}_3 along \mathbf{a}_1 . In our benchmark case of a 24-atom Mg supercell, we need a minimum \mathbf{k} -point mesh of $12 \times 20 \times 2$ to achieve convergence in γ_{sf} . In order to have the same density of \mathbf{k} points for the 128-atom supercells, we need to use meshes of at least $6 \times 5 \times 3$, $10 \times 5 \times 2$, and $5 \times 6 \times 3$ for the basal, and first-order and second-order pyramidal planar faults, respectively. For all our calculations, we use the non-sc method, a very dense mesh of $10 \times 10 \times 10$ \mathbf{k} points and the

TABLE II. Atomic percentage concentration of Li, Zn, or Y in ternary and binary alloys at each layer of a basal configuration [see Fig. 1(b)], as constructed by the SQS method. The first layer is at the stacking fault (interface) and the third is closer to the middle of the supercell. Basal (interface) and basal (remote) refer to the two different configurations where the Ca atom is either at the stacking fault or “remote” from it.

| Alloy | X at% per layer ($X = \text{Li, Zn, Y}$) | | | | | |
|-------------------|--|-----------------|----------------------|-----------------|-----------------|----------------------|
| | Basal (interface) | | | Basal (remote) | | |
| | 1 st | 2 nd | $\geq 3^{\text{rd}}$ | 1 st | 2 nd | $\geq 3^{\text{rd}}$ |
| tLi ₁ | 0.00 | 0.00 | 0.78 | 0.00 | 0.00 | 0.78 |
| tLi ₂ | 1.56 | 0.00 | 0.00 | 0.00 | 1.56 | 0.00 |
| tLi ₄ | 0.78 | 0.00 | 2.34 | 0.78 | 0.78 | 1.56 |
| tLi ₁₇ | 3.13 | 4.69 | 5.47 | 3.13 | 4.69 | 5.47 |
| tZn ₁ | 0.78 | 0.00 | 0.00 | 0.00 | 0.00 | 0.78 |
| tZn ₂ | 1.56 | 0.00 | 0.00 | 0.78 | 0.78 | 0.00 |
| tZn ₃ | 2.34 | 0.00 | 0.00 | 1.56 | 0.78 | 0.00 |
| tZn ₂₂ | 7.81 | 4.69 | 4.69 | 3.91 | 5.47 | 7.81 |
| tY ₁ | 0.00 | 0.00 | 0.78 | 0.00 | 0.00 | 0.78 |
| tY ₂ | 0.00 | 0.78 | 0.78 | 0.78 | 0.00 | 0.78 |
| tY ₃ | 0.00 | 1.56 | 0.78 | 0.78 | 0.00 | 1.56 |
| tY ₆ | 0.00 | 1.56 | 3.13 | 1.56 | 0.00 | 3.13 |

PBE generalized gradient approximation (GGA) to calculate the exchange and correlation potential.

We present the alloys we use for our calculations in Table I. We study four different alloy compositions for three ternary alloys, Mg-Li-Ca, Mg-Zn-Ca, and Mg-Y-Ca; three low and one high (near or above the solubility limit) concentration alloying element alloys. The subscript in the alloy names shows the number of atoms of Li, Zn, or Y in the 128-atom supercell. The solubility of Ca in Mg is limited (<1 at% [51,52]) thus we only use one Ca atom in the supercell. The remaining concentration is Mg. Regardless of the concentration in the alloy, we keep the c/a ratio fixed to that of pure Mg.

We create two different configurations for each alloy. One where we place the Ca atom at the SF (“interface”) and another where Ca is at the middle of the supercell (perpendicular to the planar fault) and hence “remote” from the fault. For the allocation of the second alloying element in the supercell, we use the special quasi-random-structure (SQS) approach [53] (Fig. 1). In this way, the procedure for constructing our “interface” and “remote” supercells is first to place the Ca atoms by hand, either at the fault plane, or in a “remote” site, and subsequently place the ternary elements according to the SQS prescription. We show the alloying element distribution, depending on the Ca position (“interface” or “remote”), at each layer of a basal configuration in Table II.

In Table III, we present results for the stable stacking fault energies for pure Mg, binary Mg-0.78Ca at% (designated as bCa), and all ternary Mg alloys, for the two different configurations and the basal and pyramidal planes. In addition to the standard relaxation method, we include results from calculations of the SFE with full atomic relaxation (FAR). A similar method, more suitable for the construction of the γ surface, was initially proposed by Morris [60]. In this method,

both in- and out-of-plane atomic relaxation is permitted. Calculations with full atomic relaxation exhibit both qualitative and quantitative differences from the Vitek relaxation method [47], where only out-of-plane relaxation [27] is allowed. Qualitatively, the SFE of the pyramidal planes is predicted at a different lattice vector; it is located at $\sim 36\%$ instead of $\sim 44\%$ of the lattice vector, as predicted with the Vitek relaxation method for the pyramidal-I plane and at $\sim 54\%$ instead of $\sim 33\%$ of the lattice vector for the pyramidal-II plane, as also noted by Yin [27]. The basal plane γ_{sf} is at the same lattice vector with either method, as expected from symmetry.

Experimental measurement of SFE exhibits larger uncertainty than DFT calculations. In Ref. [59], the experimental basal SFEs for Mg hugely vary from ~ 50 to 280 mJ/m², depending on the experimental method and on the crystal type (single or polycrystal). Those values are much larger than theoretical predictions, which also strongly depend on the method and computational parameters. The variation in DFT calculations in the literature for pure Mg can be seen in Table III. Pyramidal plane SFEs for Mg have not been measured experimentally.

A. Concentration

We start our analysis by examining Table III. This table expands the results we have previously published [61] by presenting additional results firstly for Mg-Y-Ca alloys, secondly for the pyramidal-II plane for all three ternary alloys, and thirdly results for calculations with full atomic relaxation for the “remote” case. In this section, we focus our analysis on the “remote” case where the Ca atom is far from the stacking fault. All results are grouped and visualized in Fig. 3, showing the trends in the change of the SFE as the alloying element concentration increases.

For the Mg-Li-Ca alloys (tLi alloys), we observe a sharp increase in the basal SFE with increasing concentration of Li, reaching a value twice as large as in pure Mg for the saturated alloy. On the contrary, the SFEs in both pyramidal planes are lower than those of pure Mg (apart from tLi₄) and are reduced with increasing Li concentration. The change in the SFE of the tLi₂₂ alloy comparing to pure Mg is 100%, -13% , and -21% for the basal, pyramidal I and II planes, respectively.

For the Mg-Zn-Ca alloys (tZn alloys), we observe a different behavior. The basal SFE for low concentration alloys (tZn₁₋₃) is slightly higher than that of pure Mg ($\sim 12\%$) but it remains in the same level as of pure Mg for the saturated alloy. This highlights the behavior of Zn in Mg alloys, where Zn does not contribute much in the basal SFE and Ca is the dominant contributor in this case. We discuss the Ca contribution extensively in Sec. III D. For both pyramidal planes, we observe a small decrease in the SFEs for the low-concentration alloys and a sharp decrease for the saturated alloy (-42% and -24% for the pyramidal planes, respectively). The Zn contribution in the SFE for Mg-Zn-Ca alloys is higher in the pyramidal planes than the basal plane, especially for high Zn concentration.

In Mg-Y-Ca alloys (tY alloys), we observe a nonmonotonic behavior in the change of the SFE as the Y concentration increases. Basal SFEs for the tY alloys are higher than pure Mg for low Y concentrations, regardless of the Ca position,

TABLE III. Basal, pyramidal-I, and pyramidal-II stable SFEs of Mg, Mg-0.78Ca at% (designated below as bCa), and Mg ternary alloys, as described in Table I, for the two different configurations “interface” and “remote.” Additionally, we include results from full atomic relaxation (FAR) calculations for Mg, Mg-0.78Ca, and the pyramidal-II plane “remote” for all alloys. We calculate the SFE with the non-sc method based on the HF approximation. All values are in mJ/m².

| Alloy | Basal [1 $\bar{1}$ 00] (0001) | | Pyramidal I 1/3[$\bar{1}$ $\bar{1}$ 23] (10 $\bar{1}$ 1) | | Pyramidal II 1/3[$\bar{1}$ $\bar{1}$ 23] (11 $\bar{2}$ 2) | |
|--------------------|----------------------------------|---------------------|--|--------------------|---|--------------------|
| | Interface | Remote | Interface | Remote | Interface | Remote (FAR) |
| Mg | | 32.1 ^{a,b} | | 220.3 ^c | | 246.0 ^d |
| Mg ^{FAR} | | 32.1 ^e | | 158.8 ^f | | 158.5 ^g |
| bCa | 31.0 ^h | 40.3 | 224.4 | 209.4 | 269.1 | 245.5 |
| bCa ^{FAR} | 29.2 ⁱ | 38.2 | | 143.9 | | 157.4 |
| tLi ₁ | 30.1 | 36.9 | 248.0 | 203.5 | 284.9 | 226.6 (142.7) |
| tLi ₂ | 40.7 | 45.2 | 228.2 | 213.9 | 279.0 | 220.7 (140.3) |
| tLi ₄ | 30.5 | 45.3 | 241.6 | 192.5 | 264.3 | 251.8 (144.7) |
| tLi ₁₇ | 50.7 | 64.1 | 261.7 | 189.8 | 231.9 | 192.5 (126.2) |
| tZn ₁ | 31.2 ^j | 36.5 | 322.1 | 208.5 | 277.5 | 227.9 (143.8) |
| tZn ₂ | 26.6 | 36.3 | 318.0 | 205.1 | 287.1 | 219.1 (131.0) |
| tZn ₃ | 28.0 | 36.0 | 317.3 | 202.3 | 278.2 | 218.4 (132.6) |
| tZn ₂₂ | 13.1 | 31.6 | 270.6 | 126.3 | 199.4 | 185.8 (100.9) |
| tY ₁ | 32.2 | 45.5 | 247.0 | 210.2 | 321.6 | 217.1 (142.1) |
| tY ₂ | 40.4 | 44.9 | 272.0 | 193.5 | 251.6 | 202.9 (132.5) |
| tY ₃ | 44.6 | 36.1 | 290.5 | 215.2 | 330.5 | 192.6 (113.6) |
| tY ₆ | 25.7 | 30.5 | 294.2 | 266.9 | 319.1 | 216.1 (132.5) |

^a33.0 calculated with the sc method.

^bLiterature: 44 [54], 36 [55], 34 [56], 33.8 [31], 37 [32], ~41 [34], 30.0 [57].

^cLiterature: 180 [58].

^dLiterature: 298 [32], 236 [58].

^eLiterature: 34 [27], 30.0 (including cell shape and volume relaxation) [59].

^fLiterature: 161 [27].

^gLiterature: 165 [27].

^hLiterature: 21.8 [57].

ⁱLiterature: 23.8 (including cell shape and volume relaxation) [59].

^jLiterature: ~38 [34].

and they decrease to a value lower than pure Mg for the saturated alloy tY₆. Pyramidal SFEs exhibit opposite behavior to basal-plane SFEs. The low Y concentration “remote” pyramidal SFEs are lower than in pure Mg (2%–12% and 11%–21% decrease for pyramidal I and II, respectively) but they become higher for the saturated alloys. The “interface” pyramidal SFEs exhibit a linear increase, always higher than in pure Mg, showing that Ca segregation in this category of alloys is not favoured in the pyramidal planes. The tY₃ “remote” pyramidal II SFE is the lowest of all pyramidal SFEs of tY alloys.

As expected, the SFEs from simulations with full atomic relaxation are lower than those with only out-of-plane atomic relaxation. The Mg pyramidal I and II full atomic relaxation SFEs are reduced by ~28% and ~36%, respectively, comparing to only out-of-plane atomic relaxation. Interestingly enough, the fully relaxed SFEs of Mg are the same for both pyramidal planes. Calculations of the pyramidal-II “remote” with full atomic relaxation SFEs for the ternary alloys show a large reduction of 35% to 43%. All SFEs with full atomic relaxation follow the same qualitative trends as the SFEs with only out-of-plane atomic relaxation, hence similar conclusions can be drawn.

B. Anisotropy

In Table IV, we have calculated the ratio of the pyramidal over the basal stable SFEs. For pure Mg this value is 6.9 and 7.7 for pyramidal I and II planes respectively (and 4.9 for calculations with full atomic relaxation for both planes), showing the large anisotropy. For the studied ternary alloys, we have calculated this ratio for both “interface” and “remote” configurations. In this section, we examine and discuss the case where Ca is “remote” from the fault, as Ca segregation is unfavourable in pyramidal planes as we observe in Table III. Even though we calculate the anisotropy ratio only for stable SFEs, we presume that it can be used as an indicator of anisotropy in a large number of mechanical properties associated with both stable and unstable SFEs. A monotonic behavior is usually observed in the change of the stable and unstable basal SFEs in Mg alloys comparing to pure Mg [30,31].

In Table IV, we see that the anisotropy for Mg-Li-Ca alloys is lower than in pure Mg for any concentration for both pyramidal planes. Especially for the saturated alloy tLi₂₂ the anisotropy is greatly reduced to more than half of that of pure Mg. If we compare with values of the SFE from Table III we see that the reduction of anisotropy in this category of

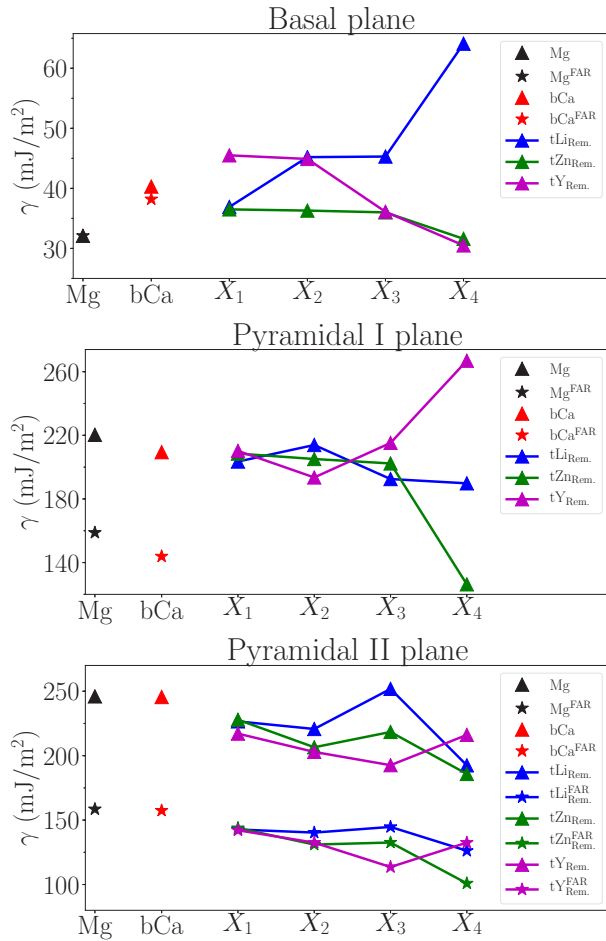


FIG. 3. Stable stacking fault energies of the three planar faults, for Mg, Mg-0.78Ca at% (designated as bCa), and three ternary alloys in four different concentrations (where $X_{i=1-4}$ refers to the increasing concentration tLi, tZn, and tY alloys, as i increases). The upright triangles refer to the “remote” case and the stars to simulations with full atomic relaxation (FAR).

alloys is due to the large increase of the basal SFEs rather than the moderate decrease of the pyramidal SFEs. This makes Mg-Li-Ca alloys suitable for applications where high strength and lightweight alloys are required, as has also been reported before [62] for a Mg-Li-Ca alloy similar to our tLi₂₂ alloy.

As in Mg-Li-Ca alloys, the anisotropy of all Mg-Zn-Ca alloys is lower than in pure Mg. The ratio $\gamma_{sf}^{PyrI}/\gamma_{sf}^{Bas}$ remains constant for the low concentration alloys (tZn₁₋₃) and it sharply reduces by 45% for the saturated alloy. The Zn concentration affects less the $\gamma_{sf}^{PyrII}/\gamma_{sf}^{Bas}$ ratio. The reduction in the anisotropy ratio for Mg-Zn-Ca alloys is mainly due to the decrease of the pyramidal SFEs combined with the increase of the basal SFEs. The large decrease of the anisotropy ratio for the saturated alloy is due to the over 42% and 24% decrease in pyramidal I and II SFEs, respectively, possibly inhibiting the extent of easy glide. The large contribution of Zn could potentially be exploited to tackle the large industrial issue of low formability of Mg alloys.

Increase in anisotropy is observed in the Mg-Y-Ca alloys as the Y concentration increases. In this case, low anisotropy

TABLE IV. Ratio of stable SFEs of the pyramidal I and II planes over the basal plane. This ratio demonstrates the magnitude of anisotropy between the three major slip planes in Mg alloys and the effect of solid-solution. As in Table III, bCa refers to binary Mg-0.78Ca at%. The values in parentheses refer to simulations with full atomic relaxation (FAR).

| Alloy | $\gamma_{sf}^{PyrI}/\gamma_{sf}^{Bas}$ | | $\gamma_{sf}^{PyrII}/\gamma_{sf}^{Bas}$ | |
|-------------------|--|-----------|---|-----------|
| | Interface | Remote | Interface | Remote |
| Mg | | 6.9 (4.9) | | 7.7 (4.9) |
| bCa | 7.2 | 5.2 (3.8) | 8.7 | 6.1 (4.1) |
| tLi ₁ | 8.2 | 5.5 | 9.5 | 6.1 |
| tLi ₂ | 5.6 | 4.7 | 6.9 | 4.9 |
| tLi ₄ | 7.9 | 4.2 | 8.7 | 5.5 |
| tLi ₁₇ | 5.2 | 3.0 | 4.6 | 3.0 |
| tZn ₁ | 10.3 | 5.7 | 8.9 | 6.2 |
| tZn ₂ | 11.9 | 5.7 | 10.8 | 5.7 |
| tZn ₃ | 11.3 | 5.6 | 9.9 | 6.1 |
| tZn ₂₂ | 20.6 | 4.0 | 15.2 | 5.9 |
| tY ₁ | 7.7 | 4.6 | 10.0 | 4.8 |
| tY ₂ | 6.7 | 4.3 | 6.2 | 4.5 |
| tY ₃ | 6.5 | 6.0 | 7.4 | 5.3 |
| tY ₆ | 11.4 | 8.7 | 12.4 | 7.1 |

is mainly observed for low Y concentration alloys and in particular for the tY₂ alloy. The decrease of anisotropy in Mg-Y-Ca alloys is due to the decrease of the pyramidal plane SFEs. The anisotropy factor is higher for the saturated alloy tY₆. For all alloys, higher values of the anisotropy factor are recorded when Ca is at the stacking fault.

C. Alloy design

Something that is often neglected to be examined is the impact of the atomic-scale microstructure on alloy design, which is generally only accessible through simulations. As described earlier, for each alloy we have calculated two different configurations by distributing the Ca atom in a different position. This expands the general approach of studying SFEs of alloys, where usually only the case of the alloying element being placed at the stacking fault is considered.

In this study, the effect of atomic-scale microstructure is reflected in the value of the SFEs by comparing the “interface” and “remote” SFEs of an alloy, as we demonstrate in Table III. For all alloys, we observe a rather generic trend in their SFEs. For the basal plane, the “interface” SFEs are almost always lower than the “remote” SFEs (exception is the tY₃ alloy). On the other hand, the pyramidal “interface” SFEs are always higher than the “remote” SFEs. This shows the tendency of alloying elements to segregate to the basal-plane stacking fault. Segregation to grain boundaries has been observed experimentally for Mg-Li-Ca alloys [63] and Mg-Zn-Ca alloys [64]. For slip along the pyramidal planes, we observe that segregation of alloying elements to stacking faults is highly unfavourable.

Although a direct comparison cannot be made for all alloys, with the guidance of Table II, we examine which of the alloying elements (Ca or Li/Zn/Y) contribute more in the change of the “interface” basal SFEs. We observe that the tLi₁,

TABLE V. Basal stable SFEs of ternary and the associated binary alloys (designated with a prefix “b”). Their atomic composition and per layer distribution in the supercell are described in Tables I and II. bCa is Mg-0.78Ca at%. The “interface” (Int.) and “remote” (Rem.) refer to the Ca position in the supercell for the ternary alloys and the corresponding configuration for their associated binary alloys. $\gamma_{sf}^{Mg} = 32.1 \text{ mJ/m}^2$. All values are in mJ/m^2 .

| Ternary alloy | Int. | Rem. | Binary alloy | Int. | Rem. |
|-------------------|------|------|-------------------|------|------|
| | | | bCa | 31.0 | 40.3 |
| tLi ₁ | 30.1 | 36.9 | bLi ₁ | 35.9 | 31.4 |
| tLi ₂ | 40.7 | 45.2 | bLi ₂ | 39.5 | 36.6 |
| tLi ₄ | 30.5 | 45.3 | bLi ₄ | 35.2 | 36.1 |
| tLi ₁₇ | 50.7 | 64.1 | bLi ₁₇ | 51.1 | 69.0 |
| tZn ₁ | 31.2 | 36.5 | bZn ₁ | 31.8 | 31.9 |
| tZn ₂ | 26.6 | 36.3 | bZn ₂ | 31.5 | 31.5 |
| tZn ₃ | 28.0 | 36.0 | bZn ₃ | 31.7 | 31.2 |
| tZn ₂₂ | 13.1 | 31.6 | bZn ₂₂ | 13.1 | 24.7 |
| tY ₁ | 32.2 | 45.5 | bY ₁ | 38.7 | 41.1 |
| tY ₂ | 40.4 | 44.9 | bY ₂ | 44.1 | 37.0 |
| tY ₃ | 44.6 | 36.1 | bY ₃ | 41.6 | 36.5 |
| tY ₆ | 25.7 | 30.5 | bY ₆ | 38.4 | 28.7 |

tLi₄, tLi₂₂, and tY₁ alloys have the same atomic percentage concentration of alloying elements at the first layer (stacking fault) either when Ca is at the stacking fault or far from it. For those alloys, Ca is the main contributor for lowering the “interface” basal SFE. In the next paragraphs we present and compare results for binary alloys. We will be able to discuss the contribution of each element in the alloy, and in particular of Ca, and their tendency to segregate.

D. Ca contribution

To understand the effect of Ca, we have calculated the basal SFEs for binary Mg alloys without Ca and compared them with results from our ternary alloys. For calculations in binary alloys we have used the same configurations and solute distribution as in ternary alloys (as described in Tables I and II) and replaced the Ca atom with Mg. Therefore the “interface” and “remote” binary configurations are inherited from the ternary configurations as created with the SQS method when Ca was present. The atomic percentage compositions of binary alloys (using the ternary alloys’ notation with a prefix “b”) are Mg- x Li, where x is 0.78, 1.56, 3.13, and 13.28 at% (bLi_{1,2,4,17}); Mg- x Zn alloys, where x is 0.78, 1.56, 2.34, and 17.19 at% (bZn_{1,2,3,22}); Mg- x Y alloys, where x is 0.78, 1.56, 2.34, and 4.69 at% (bY_{1,2,3,6}). We present the basal SFEs for binary alloys in Table V.

We observe that binary Mg- x Li alloys increase the basal SFEs compared to pure Mg. Similar qualitative results can be found in the literature [30,59,65] for the “interface” case. In comparison with the ternary alloys, the increase of the basal SFEs for the binary alloys is smaller. The change in the “remote” basal SFE of the binary alloys is of 15%–20%, depending on the Li concentration, and it can be considered as the Ca contribution in Mg-Li-Ca alloys. For the saturated alloy, the Li atoms seem to dominate the contribution in basal SFE.

The tendency of Ca to increase the “remote” basal SFE is confirmed by our calculations for a low Ca concentration binary Mg-0.78Ca at% alloy. The basal SFEs are 31.0 and 40.3 mJ/m^2 (29.2 and 38.2 for simulations with full atomic relaxation) when the Ca atom is at the fault or “remote” from it, respectively. The lower “interface” basal SFE (with or without full atomic relaxation), compared with pure Mg, agrees qualitatively with results in the literature [57,59]. To our knowledge, there are no previous studies of Mg-Ca alloys where the Ca atom is placed far from the stacking fault. The lower “interface” basal SFE may also explain the tendency of Ca to segregate in grain boundaries [64,66].

For the binary Mg- x Zn alloys we observe that the SFEs of the low Zn concentration alloys are similar to those of pure Mg and only the saturated alloy reduces the basal SFE. Qualitatively similar results can be found in the literature [30,31,33,59,65]. Comparing with the ternary alloys, there is a decrease of $\sim 13\%$ in the “remote” γ_{sf} for the low Zn concentration binary alloys, which can be attributed to Ca absence. The decrease is significantly larger for the saturated alloy.

Zn additions in nonbinary Mg alloys seem to have a significant role in some key mechanical properties. Mg-Zn-RE alloys, with solute Zn and low concentration of rare earth, have been found to weaken the texture in the basal plane [67,68], and have higher strength and improved ductility [67,69,70]. Mg-Zn-Ca alloys are attractive due to their good mechanical properties and biocompatibility [16,17,71]. It has been found that specific concentrations of Zn and Ca lead to low anisotropy, and have higher strength and formability than other commercial alloys [72].

More specifically Yuasa *et al.* [34] have studied the basal SFEs of a ternary Mg-Zn-Ca alloy, similar to our tZn₁ alloy, and the binary Mg-Zn and Mg-Ca alloys trying to explain the high-stretch formability of Mg-Zn-Ca alloys. Their calculated basal SFEs are in good qualitative agreement with our results, showing improved plastic anisotropy and justifying the good formability. According to Zeng *et al.* [64], Ca and Zn co-segregation is expected to reduce even more the grain boundary energy than an individual Zn or Ca segregation. Despite the small reduction, we do observe a reduced basal “interface” SFEs for the tZn_{2,3,22} alloys comparing to Ca-free binary bZn_{2,3,22} alloys.

The basal SFEs of binary Mg-Y alloys exhibit a qualitatively similar variation as in ternary Mg-Y-Ca alloys. Comparing the “remote” basal SFEs of binary and ternary alloys we estimate the average change to be $\sim 9\%$ due to Ca contribution. In contrast with the previous two studied binary alloys, in this case the Ca contribution seems to be minor. The basal SFE of low Y concentration binary Mg-Y alloys has been extensively studied in the literature and compared against pure Mg, showing a large reduction when Y is at the stacking fault [30,31,33,57,59]. As we see in Table II, the Y-containing alloys do not have any Y atoms at the stacking fault, thus we cannot compare directly with our results. The “remote” tY_{2,3,6} and bY_{2,3,6} alloys contain Y atoms both at the stacking fault and far from it. Those alloys exhibit reducing basal SFEs as Y concentration increases, which is in accordance with the literature.

Summarizing the previous results, we see that the Ca contribution in the basal SFE strongly depends on the alloying

elements in the system. The greater Ca contribution is exhibited for the alloys, which contain small atomic radius Li atoms, while the smallest is for the alloys with large atomic radius Y atoms. Despite the small statistical sample, we do observe a trend in the contribution of Ca which depends on the atomic size of the other elements. We conclude that the atomic level role of Ca in enhancing the properties of Mg alloys is essentially due to an atomic size effect (or atomic “misfit”). Similarly, it is the atomic size effect along with the chemical bonding that are the main contribution mechanisms of low concentration rare earths in Mg alloys during the solid-solution strengthening process [14,73–76].

IV. CONCLUSIONS

We performed high-quality non-sc DFT calculations to predict the stable stacking fault energies for three ternary Mg alloys along the basal, pyramidal I and II planes. We have showcased that the non-sc DFT calculations give an accurate prediction of the γ_{sf} and also greatly improve the computational efficiency. This allows us to examine a large number of different concentration binary and ternary alloys and also explore the prospects of the alloy design process by testing two different configurations for each alloy. From the study of the SFE along the three glide planes we are able to conclude that:

(1) There is a direct effect of the alloying concentration on the SFE which depends on the alloying element and could either increase or decrease the value of stable stacking fault energy. When Ca is “remote” from the stacking fault, Mg-Li-Ca alloys exhibit greatly increased basal SFEs while the saturated Mg-Zn-Ca alloy exhibits greatly reduced pyramidal SFEs. Additionally, all ternary alloys exhibit reduced pyramidal SFEs comparing to pure Mg, apart from some minor exceptions. Calculations with full atomic relaxation (FAR) predict a lower value for all SFEs. Nevertheless, these calculations show a similar qualitative dependency on the alloying concentration with only out-of-plane atomic relaxation simulations. In contrast, the location of the minimum in the SFE of $\langle c + a \rangle$ faults is shifted.

(2) We use the $\gamma_{sf}^{PyrI}/\gamma_{sf}^{Bas}$ and $\gamma_{sf}^{PyrII}/\gamma_{sf}^{Bas}$ ratios to discuss anisotropy in mechanical properties of Mg alloys. For all Mg-Li-Ca and Mg-Zn-Ca alloys, the anisotropy is greatly

reduced when Ca is “remote” from the stacking fault, especially for the tLi₂₂ alloy where the anisotropy is less than half of pure Mg. We observe a similar reduction for the low Y concentration Mg-Y-Ca alloys. The saturated alloy tY₆ is the only alloy where anisotropy increases. By comparing the anisotropy ratio and the mechanism, it is modified we have identified that Mg-Li-Ca alloys can increase tensile strength, hence reduce elongation, in the basal plane, and Mg-Zn-Ca alloys can potentially increase formability.

(3) The use of the SQS method shows the impact of atomic-scale microstructure on alloy design. The SFEs of “interface” and “remote” binary alloys greatly vary despite the same concentration of the alloying element. This highlights the importance of examining thoroughly the microstructure when studying alloy properties.

(4) The position of Ca in the supercell affects strongly the SFE. For the studied ternary alloys we observe mainly a decrease in the basal SFEs and always an increase in the pyramidal SFEs when Ca is at the stacking fault. By studying the two different positions of Ca, we can estimate the tendency of the solutes to segregate to stacking faults or grain boundaries. Segregation of solutes to stacking faults in Mg alloys seems to be favorable at the basal plane but not at the pyramidal planes.

(5) By comparing the change in the basal stable stacking fault energy of ternary and binary alloys, we are able to estimate the contribution of Ca. The average Ca contribution on the basal SFEs of the ternary alloys in regard to the second alloying element in the alloy, varies as follows: Li > Zn > Y. This shows that the large atomic radius Ca atom dominates the contribution when smaller atoms are present, showing an apparent atomic radius size effect.

ACKNOWLEDGMENTS

We would like to thank D. Guan and W. M. Rainforth of Sheffield University and Mark Turski of Luxfer MEL Technologies for helpful discussions. This work is funded by the EPSRC “Designing Alloys for Resource Efficiency” (DARE) research programme (EP/L025213/1). We are grateful to the UK Materials and Molecular Modelling Hub for computational resources, which is partially funded by EPSRC (EP/P020194/1).

-
- [1] I. J. Polmear, *Mater. Sci. Technol.* **10**, 1 (1994).
 [2] Y. Lü, Q. Wang, X. Zeng, W. Ding, C. Zhai, and Y. Zhu, *Mater. Sci. Eng. A* **278**, 66 (2000).
 [3] L. Rokhlin, *Magnesium Alloys Containing Rare Earth Metals: Structure and Properties*, Advances in Metallic Alloys (CRC Press, Taylor & Francis Group, London, 2003).
 [4] Y. Wang and J. C. Huang, *Mater. Chem. Phys.* **81**, 11 (2003).
 [5] S. Agnew and J. Nie, *Scr. Mater.* **63**, 671 (2010).
 [6] K. Hantzsche, J. Bohlen, J. Wendt, K. Kainer, S. Yi, and D. Letzig, *Scr. Mater.* **63**, 725 (2010).
 [7] A. Chapuis and J. H. Driver, *Acta Mater.* **59**, 1986 (2011).
 [8] T. Al-Samman and X. Li, *Mater. Sci. Eng. A* **528**, 3809 (2011).
 [9] J. Hirsch and T. Al-Samman, *Acta Mater.* **61**, 818 (2013).
 [10] D. Griffiths, *Mater. Sci. Technol.* **31**, 10 (2015).
 [11] T. Laser, C. Hartig, M. Nürnberg, D. Letzig, and R. Bormann, *Acta Mater.* **56**, 2791 (2008).
 [12] N. Stanford, *Mater. Sci. Eng., A* **527**, 2669 (2010).
 [13] J. P. Hadorn, K. Hantzsche, S. Yi, J. Bohlen, D. Letzig, J. A. Wollmershauser, and S. R. Agnew, *Metall. Mater. Trans. A* **43**, 1347 (2012).
 [14] J. D. Robson, *Metall. Mater. Trans. A* **45**, 3205 (2014).
 [15] S. Agnew, M. Yoo, and C. Tomé, *Acta Mater.* **49**, 4277 (2001).
 [16] H. Wang, S. Guan, X. Wang, C. Ren, and L. Wang, *Acta Biomaterialia* **6**, 1743 (2010).
 [17] Y. Sun, B. Zhang, Y. Wang, L. Geng, and X. Jiao, *Mater. Des.* **34**, 58 (2012).

- [18] W. Qudong, C. Wenzhou, Z. Xiaoqin, L. Yizhen, D. Wenjiang, Z. Yanping, X. Xiaoping, and M. Mabuchi, *J. Mater. Sci.* **36**, 3035 (2001).
- [19] A. Luo, *Int. Mater. Rev.* **49**, 13 (2004).
- [20] K. Hirai, H. Somekawa, Y. Takigawa, and K. Higashiothers, *Mater. Sci. Eng., A* **403**, 276 (2005).
- [21] L. Han, H. Hu, and D. O. Northwood, *Mater. Lett.* **62**, 381 (2008).
- [22] S. Xu, N. Matsumoto, K. Yamamoto, S. Kamado, T. Honma, and Y. Kojima, *Mater. Sci. Eng., A* **509**, 105 (2009).
- [23] L. Geng, B. Zhang, A. Li, and C. Dong, *Mater. Lett.* **63**, 557 (2009).
- [24] J. Jayaraj, C. Mendis, T. Ohkubo, K. Oh-ishi, and K. Hono, *Scr. Mater.* **63**, 831 (2010).
- [25] B. Zhang, L. Geng, L. Huang, X. Zhang, and C. Dong, *Scr. Mater.* **63**, 1024 (2010).
- [26] Y. Chino, T. Ueda, Y. Otomatsu, K. Sassa, X. Huang, K. Suzuki, and M. Mabuchi, *Mater. Trans.* **52**, 1477 (2011).
- [27] B. Yin, Z. Wu, and W. Curtin, *Acta Mater.* **123**, 223 (2017).
- [28] B. Yin, Z. Wu, and W. Curtin, *Acta Mater.* **136**, 249 (2017).
- [29] Z. Wu, R. Ahmad, B. Yin, S. Sandlöbes, and W. A. Curtin, *Science* **359**, 447 (2018).
- [30] M. Muzyk, Z. Pakiela, and K. Kurzydowski, *Scr. Mater.* **66**, 219 (2012).
- [31] Q. Zhang, L. Fu, T.-W. Fan, B.-Y. Tang, L.-M. Peng, and W.-J. Ding, *Physica B (Amsterdam)* **416**, 39 (2013).
- [32] Z. Pei, L.-F. Zhu, M. Friák, S. Sandlöbes, J. von Pezold, H. W. Sheng, C. P. Race, S. Zaeferrer, B. Svendsen, D. Raabe, and J. Neugebauer, *New J. Phys.* **15**, 043020 (2013).
- [33] Z. Pei, D. Ma, M. Friák, B. Svendsen, D. Raabe, and J. Neugebauer, *Phys. Rev. B* **92**, 064107 (2015).
- [34] M. Yuasa, M. Hayashi, M. Mabuchi, and Y. Chino, *Acta Mater.* **65**, 207 (2014).
- [35] S. Sandlöbes, M. Friák, S. Korte-Kerzel, Z. Pei, J. Neugebauer, and D. Raabe, *Sci. Rep.* **7**, 10458 (2017).
- [36] J. Harris, *Phys. Rev. B* **31**, 1770 (1985).
- [37] W. M. C. Foulkes and R. Haydock, *Phys. Rev. B* **39**, 12520 (1989).
- [38] P. Hohenberg and W. Kohn, *Phys. Rev.* **136**, B864 (1964).
- [39] W. Kohn and L. J. Sham, *Phys. Rev.* **140**, A1133 (1965).
- [40] A. J. Read and R. J. Needs, *J. Phys.: Condens. Matter* **1**, 7565 (1989).
- [41] H. M. Polatoglou and M. Methfessel, *Phys. Rev. B* **41**, 5898 (1990).
- [42] M. van Schilfgaarde, A. T. Paxton, A. Pasturel, and M. Methfessel, *MRS Proc.* **186**, 107 (1990).
- [43] F. W. Averill and G. S. Painter, *Phys. Rev. B* **41**, 10344 (1990).
- [44] N. Chetty, K. W. Jacobsen, and J. K. Nørskov, *J. Phys.: Condens. Matter* **3**, 5437 (1991).
- [45] B. Farid, V. Heine, G. E. Engel, and I. J. Robertson, *Phys. Rev. B* **48**, 11602 (1993).
- [46] G. D. Bellchambers and F. R. Manby, *J. Chem. Phys.* **135**, 084105 (2011).
- [47] V. Vitek, *Philos. Mag. A* **18**, 773 (1968).
- [48] “Questaal”, www.questaal.org.
- [49] Y. Wang, L.-Q. Chen, Z.-K. Liu, and S. Mathaudhu, *Scr. Mater.* **62**, 646 (2010).
- [50] F. C. Frank, *Acta Crystallogr.* **18**, 862 (1965).
- [51] A. A. Nayeab-Hashemi and J. B. Clark, *Bull. Alloy Phase Diagrams* **8**, 58 (1987).
- [52] M. Mezbahul-Islam, A. O. Mostafa, and M. Medraj, *J. Mater.* **2014**, 704283 (2014).
- [53] A. Zunger, S.-H. Wei, L. G. Ferreira, and J. E. Bernard, *Phys. Rev. Lett.* **65**, 353 (1990).
- [54] N. Chetty and M. Weinert, *Phys. Rev. B* **56**, 10844 (1997).
- [55] A. Smith, *Surf. Sci.* **601**, 5762 (2007).
- [56] J. A. Yasi, T. Nogaret, D. R. Trinkle, Y. Qi, L. G. Hector Jr., and W. A. Curtin, *Modell. Simul. Mater. Sci. Eng.* **17**, 055012 (2009).
- [57] Y. Wu, S. Li, Z. Ding, W. Liu, Y. Zhao, and Y. Zhu, *Scr. Mater.* **112**, 101 (2016).
- [58] T. Nogaret, W. Curtin, J. Yasi, L. Hector, and D. Trinkle, *Acta Mater.* **58**, 4332 (2010).
- [59] S. L. Shang, W. Wang, B. Zhou, Y. Wang, K. Darling, L. Kecskes, S. Mathaudhu, and Z. Liu, *Acta Mater.* **67**, 168 (2014).
- [60] J. R. Morris, J. Scharff, K. M. Ho, D. E. Turner, Y. Y. Ye, and M. H. Yoo, *Philos. Mag. A* **76**, 1065 (1997).
- [61] E. I. Andritsos, G. C. G. Skinner, and A. T. Paxton, in *Magnesium Technology 2018* (Springer, Cham, 2018), pp. 63–69.
- [62] S. Nene, B. Kashyap, N. Prabhu, Y. Estrin, and T. Al-Samman, *J. Alloys Compd.* **615**, 501 (2014).
- [63] R.-C. Zeng, L. Sun, Y.-F. Zheng, H.-Z. Cui, and E.-H. Han, *Corrosion Sci.* **79**, 69 (2014).
- [64] Z. Zeng, Y. Zhu, S. Xu, M. Bian, C. Davies, N. Birbilis, and J. Nie, *Acta Mater.* **105**, 479 (2016).
- [65] J. Han, X. Su, Z.-H. Jin, and Y. Zhu, *Scr. Mater.* **64**, 693 (2011).
- [66] S. Liu, B. Li, X. Wang, W. Su, and H. Han, *J. Mater. Process. Technol.* **209**, 3999 (2009).
- [67] J. Bohlen, M. R. Nürnberg, J. W. Senn, D. Letzig, and S. R. Agnew, *Acta Mater.* **55**, 2101 (2007).
- [68] J. D. Robson, *Mater. Sci. Technol.* **31**, 257 (2015).
- [69] Y. Kawamura, K. Hayashi, A. Inoue, and T. Masumoto, *Mater. Trans.* **42**, 1172 (2001).
- [70] A. Inoue, Y. Kawamura, M. Matsushita, K. Hayashi, and J. Koike, *J. Mater. Res.* **16**, 1894 (2001).
- [71] J. Hofstetter, M. Becker, E. Martinelli, A. M. Weinberg, B. Mingler, H. Kilian, S. Pogatscher, P. J. Uggowitzer, and J. F. Löffler, *JOM* **66**, 566 (2014).
- [72] N. Kim, J. H. Bae, D. W. Kim, and D. H. Kim, Magnesium alloy sheet having superior formability at room temperature, and method for manufacturing same, WO Patent App. PCT/KR2011/008991 (2012), <https://patentscope.wipo.int/search/en/detail.jsf?docId=WO2012070870>.
- [73] A. Akhtar and E. Teghtsoonian, *Philos. Mag. A* **25**, 897 (1972).
- [74] L. Gao, R. Chen, and E. Han, *J. Alloys Compd.* **481**, 379 (2009).
- [75] J. A. Yasi, L. G. Hector, and D. R. Trinkle, *Acta Mater.* **58**, 5704 (2010).
- [76] Z. Lü, J. Zhou, Z. Sun, and R. Chen, *Chin. Sci. Bull.* **58**, 816 (2013).